

Pentagonal nanowires from topological crystalline insulators: a platform for intrinsic core-shell nanowires and higher-order topology

Ghulam Hussain^{1,2}, Giuseppe Cuono^{1,3}, Piotr Dziawa⁴, Dorota Janaszko⁴, Janusz Sadowski⁴, Slawomir Kret⁴, Bogusława Kurowska⁴, Jakub Polaczyński¹, Kinga Warda^{1,5}, Shahid Sattar⁶, Carlo M. Canali⁶, Alexander Lau¹, Wojciech Brzezicki¹, Tomasz Story^{1,4} and Carmine Autieri^{1,*}

¹*International Research Centre MagTop, Institute of Physics,
Polish Academy of Sciences, Aleja Lotników 32/46, PL-02668 Warsaw, Poland*

²*Institute for Advanced Study, Shenzhen University, Shenzhen 518060, China*

³*Consiglio Nazionale delle Ricerche (CNR-SPIN),*

Unità di Ricerca presso Terzi c/o Università "G. D'Annunzio", 66100 Chieti, Italy

⁴*Institute of Physics, Polish Academy of Sciences,
Aleja Lotników 32/46, PL-02668 Warsaw, Poland*

⁵*Faculty of Applied Physics and Mathematics, Gdansk University of Technology, Gdańsk 80-233, Poland*

⁶*Department of Physics and Electrical Engineering, Linnaeus University, 392 31 Kalmar, Sweden*

(Dated: January 10, 2024)

We report on the experimental realization of $\text{Pb}_{1-x}\text{Sn}_x\text{Te}$ pentagonal nanowires (NWs) with [110] orientation using molecular beam epitaxy techniques. Using first-principles calculations, we investigate the structural stability in NWs of SnTe and PbTe in three different structural phases: cubic, pentagonal with [001] orientation and pentagonal with [110] orientation. Within a semiclassical approach, we show that the interplay between ionic and covalent bonds favors the formation of pentagonal NWs. Additionally, we find that this pentagonal structure is more likely to occur in tellurides than in selenides. The disclination and twin boundary cause the electronic states originating from the NW core region to generate a conducting band connecting the valence and conduction bands, creating a symmetry-enforced metallic phase. The metallic core band has opposite slopes in the cases of Sn and Te twin boundary, while the bands from the shell are insulating. We finally study the electronic and topological properties of pentagonal NWs unveiling their potential as a new platform for higher-order topology and fractional charge. These pentagonal NWs represent a unique case of intrinsic core-shell one-dimensional nanostructures with distinct structural, electronic and topological properties between the core and the shell region.

I. INTRODUCTION

Three-dimensional topological insulators have gapped bulk states but gapless conducting edge states dictated by the bulk topological invariant and protected by the relevant symmetries. Higher-order band topological insulators (HOTIs) provide lower-dimensional boundary states as gapless hinge or corner states.¹⁻³ Within the magnetic topological insulators, the axion insulating phase is an example of higher-order topology proposed in compounds and superlattices⁴⁻⁶. Very few real materials have been proposed for the experimental realization of HOTI, two of the most popular are bismuth⁷ and cubic SnTe nanowires (NWs)⁸. Indeed, it was proposed that the cubic SnTe NWs under rhombohedral strain can host a helical higher-order topological insulator phase⁸. This is protected by both mirror and time-reversal symmetry, but no inversion symmetry is needed for helical HOTI in SnTe. The rhombohedral strain has the role of suppressing the first-order topology to make the second-order topology visible⁸. Recently, it was proposed a new route through defects or dislocations to obtain higher-order topological insulators⁹⁻¹² or fractional charges^{13,14}. In case of disclinations, the system can host strong second-order topological phases provided that local C_2 , C_4 , or C_6 symmetries protecting the topological phase are present⁹; the same happens for

one-dimensional disclinations¹⁵.

Group IV-VI semiconductors are known to display interesting characteristics, including thermoelectric effects^{16,17}, ferroelectric behavior^{18,19}, and superconducting properties^{20,21}. Notably, the identification of a topological crystalline insulating phase (TCI) in materials such as SnTe²²⁻²⁶, along with certain related substitutional compounds such as $\text{Pb}_{1-x}\text{Sn}_x\text{Te}$ ²⁷ and $\text{Pb}_{1-x}\text{Sn}_x\text{Se}$ ^{28,29}, has sparked significant interest in the realm of research. This category of materials has garnered substantial attention for further investigation. The TCI phase stands apart from the conventional topological insulating phase, as the linearly dispersing Dirac states on the high-symmetry surfaces of TCIs are protected by crystal symmetries³⁰ rather than time-reversal symmetry. Consequently, the topological invariant is also different. For example, in the case of SnTe and its alloys, the invariant is named mirror Chern number^{23,31-34} since the symmetry which protects the surface states is a reflection of the crystal with respect to (110) mirror plane. Changing the dimensions or the size (whether in a 2D or 3D configuration) of materials results in the modification of their distinctive properties. Notably, a transition from bulk³⁵⁻³⁷ to thin films³⁸⁻⁴⁰ induces property variations. A case in point is SnTe: while it behaves as a trivial insulator at reduced thicknesses, it assumes a topolog-

ical nature beyond a critical thickness^{32,41–44}, displaying strong robustness against impurity doping⁴⁵. Employing scanning tunneling microscopy and spectroscopy on $\text{Pb}_{1-x}\text{Sn}_x\text{Se}$, it was demonstrated that the (001) surface hosts large terraces interspersed with step edges of varying heights. The features of low-energy states occurring at surface atomic steps have been investigated, along with an exploration of the response of these edge channels to the stoichiometry of the alloy^{21,46–49}.

The effects of the presence of defects in the TCIs were also investigated in the literature. Possible defects are disclinations or dislocations, which naturally occur in the material during its growth. These are defects that interrupt the rotational or translational symmetry in a region of the material. Fractional electric charges were observed in disclinations^{13,50,51}, it was shown that these defects can probe higher-order topology^{7,8,52}, and the criteria for a zero-energy Majorana bound state to be present at defects was given^{53,54}. Partial-dislocation-induced topological modes in 2D and 3D higher-order topological insulators were experimentally observed⁵⁵. In the recent past, an investigation was undertaken to explore the connection between the twinning in thin films and variations in the mirror Chern number⁵⁶.

Exploring the one-dimensional (1D) case, the topological crystalline insulator SnTe NWs (NWs) emerge as even more captivating than their bulk counterparts. This enhanced intrigue arises from the amplified contribution originating from topological surface states and the effects of confinement in 1D systems^{57,58}. Diverse approaches were uncovered to produce SnTe NWs. These methods encompass the utilization of high-yield alloy nanoparticles as growth catalysts¹⁹, graphene⁵⁹ and employing single-walled carbon nanotubes to produce the smallest possible SnTe NWs⁶⁰. SnTe NWs have also been thoroughly investigated theoretically. It was shown that it is possible to obtain distinct topological states through the application of varied fields⁶¹. Notably, bulk Majorana modes appear in the presence of inversion symmetry, while the imposition of symmetry-breaking fields at the NW ends leads to the emergence of Majorana zero modes, alongside the gapping of the Majorana bulk modes⁶¹. Cubic $\text{Pb}_{1-x}\text{Sn}_x\text{Te}$ NWs have also been synthesized^{62–65}. TCI NWs can serve as a platform to confine and control Dirac fermions⁶⁶, while PbTe NWs have drawn attention due to their potential to host Majorana zero modes^{67,68}. However, the realization of Majorana's fermions is challenging as it requires the growth of NWs to be integrated with a circuit that exhibits the necessary sensitivity to monitor individual electrons as they traverse through it. All of this intricate work must be conducted at extremely low temperatures and within a magnetic field that is 10,000 times stronger than Earth's⁶⁹.

Ab initio calculations were applied to investigate ultrathin cubic NWs^{70,71} and to find the critical thicknesses at which SnTe NWs go from a trivial insulating regime to a spin-orbit insulating phase and then to the TCI phase⁷¹. Great attention was recently dedicated to 2D pentag-

onal materials in different types of the Cairo pentagonal tessellation^{72–74} and their topological properties⁷⁵. Studies are present also for 1D pentagonal materials; however, only elemental and non-ionic pentagonal NWs have been experimentally realized^{76–78} or theoretically proposed^{79–82}.

In this paper, we study the structural, electronic and topological properties of the SnTe pentagonal NWs with [110] orientation. Respect to the literature¹³, our system differs for the [110] orientation, for the periodicity along the z-direction and for hosting a core chain (CC) that produces peculiar properties. First, we report the experimental realization of $\text{Pb}_{1-x}\text{Sn}_x\text{Te}$ ionic pentagonal NWs using molecular beam epitaxy technique. Then we investigate, by means of *ab initio* and model Hamiltonian calculations, the structural, electronic and topological properties of pentagonal PbTe and SnTe NWs with anionic and cationic twin boundaries. We find that the cubic [001] NWs show a robust insulating behavior⁷¹, while the pentagonal phases are metastable with a more covalent bond. This more covalent bond brings smaller band gaps and therefore favors the topological phases. We investigate the evolution of the band gap as a function of the thickness and we study the topology of the pentagonal NWs.

The paper is organized as follows: in the next section the experimental realization of the ionic pentagonal NWs is described, and the third section is instead devoted to the theoretical investigation of the structural, electronic and topological properties of the pentagonal NWs. In the fourth and last Section, we draw our conclusions.

II. EXPERIMENTAL REALIZATION OF IONIC PENTAGONAL NANOWIRES

$\text{Pb}_{1-x}\text{Sn}_x\text{Te}$ NWs were grown using the molecular beam epitaxy (MBE) approach within a home-built apparatus furnished with solid sources of SnTe, Pb, and Te (refer to Appendix A for more comprehensive information). The NWs obtained with this method have typical lengths exceeding $1\ \mu\text{m}$, with a NW growth rate surpassing $0.5\ \mu\text{m}/\text{h}$. The NW diameters display a relatively broad range, spanning from a minimum of approximately $15\ \text{nm}$ to as much as $200\ \text{nm}$. The peak distribution rests at around $40\text{--}80\ \text{nm}$. Under these specific conditions, both varieties of NWs are observed: those manifesting a four-fold and those with a five-fold symmetry in their cross-sectional profiles (see Fig. 1a). Utilizing a Scanning Electron Microscope (SEM), we conducted observations at $5\ \text{kV}$, with magnifications ranging from 10k to $300\text{k}\times$. The SEM imagery reveals a diverse NW length, spanning from $0.7\ \mu\text{m}$ to $3\ \mu\text{m}$, while the width of the structures spans between $40\ \text{nm}$ and $150\ \text{nm}$. On the substrate, a prevalent occurrence of five-fold NWs was noted, with less frequent instances of four-fold NWs. These structures exhibit remarkable symmetry and well-defined shapes, displaying evident blocks. The NW sur-

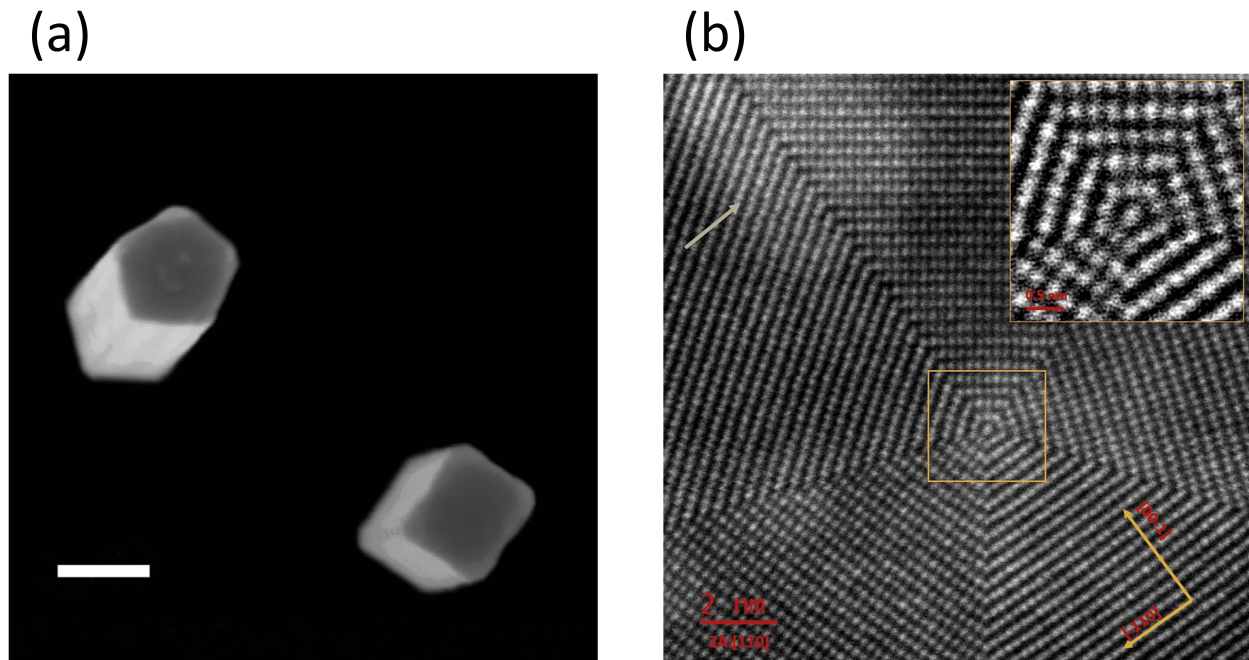


FIG. 1. (a) Scanning electron microscopy (SEM) top view image of $\text{Pb}_{1-x}\text{Sn}_x\text{Te}$ NWs at magnification 300k presenting the two possible types of cross-sections. The white scale bar is 100 nm. (b) STEM image of five-fold $\text{Pb}_{1-x}\text{Sn}_x\text{Te}$ NW with visible cubic rock salt crystal structure, and orange marked the center of the structure is zoomed in the right corner as an inset. The inset in the right corner shows a disclination with a Frank angle of $+90^\circ$ and a core chain in the center of the pentagon. The arrow indicates brighter areas related to strain fields on the twin boundary.

faces exhibit a flawlessly smooth texture devoid of imperfections.

To explore the structural attributes of the $\text{Pb}_{1-x}\text{Sn}_x\text{Te}$ NWs, we employed a transmission electron microscope. This analysis involved cross-sectioned NWs inspected along the $[110]$ zone axis, which aligns with the NW growth axis. Both scanning transmission electron microscopy (STEM) and high-resolution transmission electron microscopy modes were employed. The presence of five-fold symmetry was conclusively established. Furthermore, distinct features such as the (111) plane twin boundaries were discernible, along with brighter areas indicative of twinning. These areas are related to strain fields. In Fig. 1b), we show the STEM top view image of the five-fold $\text{Pb}_{1-x}\text{Sn}_x\text{Te}$ NW. At the core of the pentagonal structure, we have a one-dimensional disclination that follows the length of the pentagonal NW. The disclination is described by the Frank angle¹³, which in this case is $+90^\circ$. More technical details are reported in Appendix A. The twin boundaries of the experimentally obtained pentagonal nanowires seem to be composed of anion atoms. Further studies on this aspect will be presented somewhere else, while the next theoretical Sections will investigate both cation and anion twin boundaries.

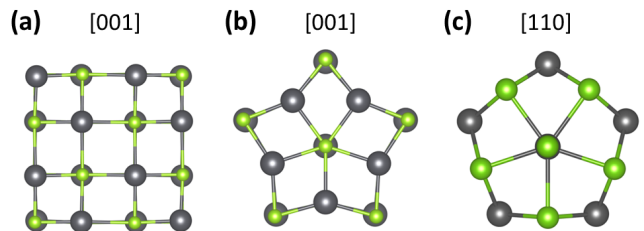


FIG. 2. Top view of the optimized SnTe NWs with (a) cubic structure oriented along $[001]$ (b) pentagonal structure along $[001]$ and (c) pentagonal structure along $[110]$ directions. The dark grey and green balls represent the Sn and Te atoms, respectively.

III. STRUCTURAL AND ELECTRONIC PROPERTIES

We divide this Section into three subsections devoting the first to the study of the structural properties, the second to the electronic band structure results and the third to the topological properties. We will work on SnTe and PbTe in the first two subsections, showing that they have the same properties at least in the thin limit. In the third and fourth sections, we will then investigate the topological properties focusing only on the SnTe NWs.

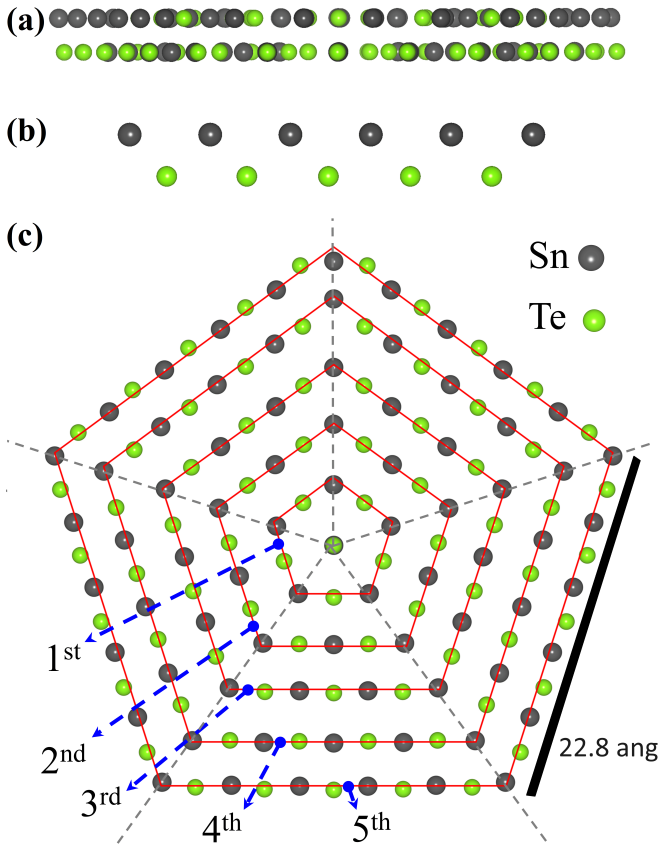


FIG. 3. (a-b) Side-tilted and top (c) views of SnTe pentagonal NWs oriented along [110] direction with cation twin boundary after structural relaxation. The rings are indicated with red lines, while the twin boundaries are highlighted with a dotted grey line. At the core, there is the one-dimensional disclination that lives in the entire length of the NWs. These crystal structures are stoichiometric since they host the same number of anions and cations. For the 5-ring structure of SnTe, the side of the pentagon (shown in black in the figure) is 22.8 Å long.

A. Structural stability of the nanowires

Using density functional theory (DFT) calculations, we compare the energetic stability of three NW crystal structures. The computational details of the calculations are reported in Appendix B. We study the cubic NWs with [001] growth orientation and the two growth orientations [001] and [110] for the pentagonal NWs. The pentagonal phases have 5 mirror planes that coincide with the plane of the twin boundaries. The pentagonal phase with [110] orientation is the phase observed in experiments. The three optimized structures of thin SnTe NWs are illustrated in Fig. 2. In Fig. 3, we report the side and top view of the [110] pentagonal NWs. The [110] pentagonal NW is composed of a core region and a shell region. The core region is composed of a core chain (CC) along the z -axis where the atoms see an environment with rotational symmetry C_5 . Additionally, there is a mirror plane at

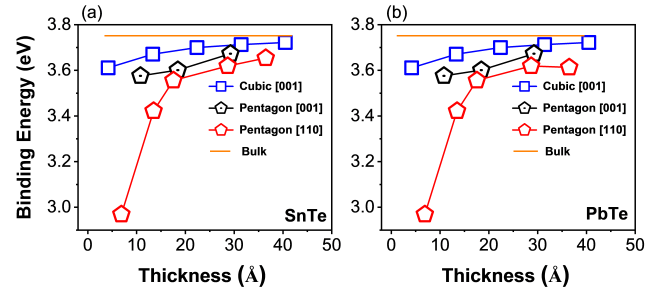


FIG. 4. Binding energy of (a) SnTe and (b) PbTe systems as a function of thickness for the two growth directions ([001] and [110]) without SOC. The horizontal orange line indicates the binding energy of the bulk case, while the blue cube, black and red pentagon represent the binding energy for the NWs cases. A thickness-dependent binding energy and hence stability can be observed. Cubic NWs have the highest binding energy after bulk, while pentagonal NWs bear the second-highest values.

$z=0$ or $z=0.5$, but there is no inversion point. The forces acting on the atoms of the core chain (one Sn and one Te atom per unit cell) are zero by symmetry. Indeed, the forces along the z -axis are compensated by the mirror symmetry while for the in-plane components, the sum of the forces of equivalent atoms located at the vertex of a regular pentagon on the center is zero. The shell region is composed of the 5 twin boundaries that separate regions where the system is locally cubic and where the atoms see locally the C_4 symmetry present in the bulk system. As we can see, the thickness of these NWs can be increased by adding more rings of corresponding atoms to the edges (sides) of each NW. In this way, the pentagonal NWs are named as 1-ring, 2-ring, 3-ring, 4-ring and 5-ring, respectively.

To examine the stability of such NW systems, the ground state binding energies per atom are calculated from the ground state total energies obtained via DFT^{79,83}:

$$E_B = \frac{n_1 E_X + n_2 E_Y - (E_{XY})}{n_1 + n_2}$$

Here, n_1 and n_2 are the numbers of cation atoms (Sn, Pb) and Te atoms in the NW, respectively. E_X and E_Y represent the ground state total energies for individual atoms (E_{Sn} , E_{Pb} , E_{Te}), and the term E_{XY} represents the total energy of the relaxed NW i.e. E_{SnTe} or E_{PbTe} . The higher the binding energy, the higher the structural stability. Fig. 4 shows the binding energy (E_B) for SnTe and PbTe NWs oriented along [001] and [110] directions, as a function of NW thickness. Also, E_B of the bulk system is portrayed as a line for comparison. It can be seen that E_B varies with the number of atoms in the NW. As the thickness of the NW increases, the binding energy also increases. This monotonic increase of E_B reflects enhancement in the stability of NWs. From Fig. 4, we observed that pentagonal NWs grown in [001] direction bear more stability and are closer to bulk value than

NWs grown along [110] orientation. However, the [001] cubic phase of NWs is observed to be the most stable one as compared to other cases. Following this analysis, the cubic phase is still the ground state for SnTe and PbTe NWs as in the bulk phase, while the pentagonal structure of SnTe and PbTe NWs is a metastable state. We calculate the binding energy as a function of the number of atoms in the unit cell, and in the limit of infinite atoms, the binding energy should tend to the value of the bulk. Indeed, the binding energy differences strongly decrease as a function of the thicknesses of NWs and could reduce to a few tens of meV for thick NWs. Therefore, it is unlikely to have thin pentagonal NWs, while they are more likely to occur for large thicknesses. Recently, it was shown that several structural configurations are possible in the case of elemental NWs with a small difference in the binding energy of few meV⁸⁴. In the ionic NWs as SnTe, the number of configurations would be certainly smaller with respect to elemental NWs due to the constraints on the alternation of anion and cation; however, as we demonstrated experimentally, it is possible to stabilize structural configurations different from the lowest energy crystal structure.

A semiclassical approach to describing the stability of ionic pentagonal NWs is reported in Appendix C. Within the semiclassical approach, for the cube, the Madelung constant is highest and particle density is lowest, indicating that the contribution of ionic bond is larger than the covalent one. In the case of hexagon, particle density is the highest and Madelung constant is the lowest indicating that the covalent bond is the dominant character of the binding. However, the pentagonal structure bears intermediate values, which implies that if the bond is partially ionic and partially covalent, the pentagonal system is expected to be the most stable one. Basically, the pentagonal structure arises from the interplay between the ionic bond and the covalent bond. The pentagonal phases of the system tend to show a more covalent bond that favors smaller gaps and metallicity. NWs based on Pb and Te would be more likely to form this unusual pentagonal structure since they will have weaker ionic bonds.

Further research is necessary to advance towards the alloyed phase $\text{Pb}_{1-x}\text{Sn}_x\text{Te}$. Our preliminary results indicate that the difference between the binding energy of the cubic and pentagonal NWs decreases to smaller values in the alloy.⁸⁵ Exploring the possibility that the CC consists solely of either Sn or Pb atoms could be a direction worth investigating. In this regard, employing genetic algorithms might predict the crystal structure and the cationic composition of the CC⁸⁴.

B. Electronic properties of the pentagonal nanowires

In general, as we decrease the thickness, we can observe a bandwidth reduction. The bandwidth reduction brings metals and topological systems into the trivial insulating

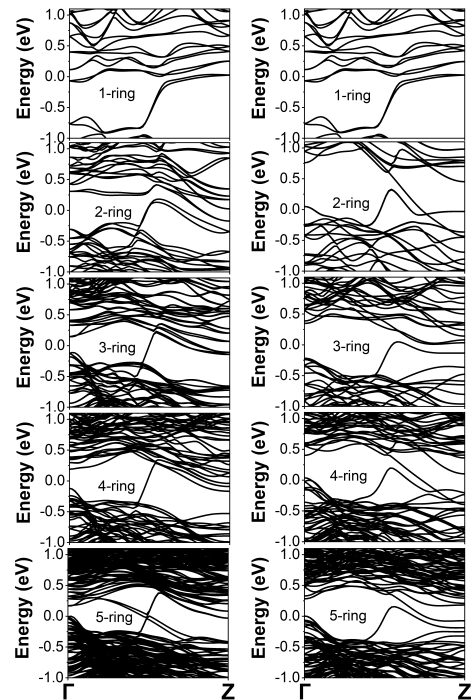


FIG. 5. Electronic band structures for [110] oriented pentagonal SnTe NWs with SOC included. (Left panel) Band structures with Sn on the twin boundaries, (right panel) and the results for Te on the twin boundaries. The band structures of 1-ring are equal in both cases since the structural relaxation brings to the same crystal structure.

phase^{71,86,87}. For the cubic PbTe NWs, the band gap decreases as the thickness increases. For the ultrathin cubic SnTe NWs, we have a trivial insulating behavior with the band gap decreasing as we increase the thickness up to the appearance of a trivial spin-orbit insulating phase, and further increasing the thickness the topological phase emerges⁷¹.

To see the effect of the thickness dependence on the electronic properties of pentagonal NWs, we considered the [110] oriented pentagonal SnTe NWs for different thicknesses. We report the electronic band structures including the SOC effects for two cases of the [110] oriented SnTe pentagonal NWs with Sn on the twin boundaries and Te on the twin boundaries. The band structures of the SnTe and PbTe pentagonal NWs without SOC included are instead shown in Appendix D, no major differences are observed between SnTe and PbTe. However, the two pentagonal NWs with different twin boundaries show different properties as observed also in [111] thin films⁵⁶. In Fig. 5 we show the two cases with different twin boundaries, where all the band structures reveal metallic behavior with bands connecting the valence and conduction electrons. While the behavior as a function of the thickness does not change for the Te twin-boundary NWs, for the 5-ring NW with Sn twin-boundary we observe an additional band connecting the valence and conduction band that seems to close and invert the band gap

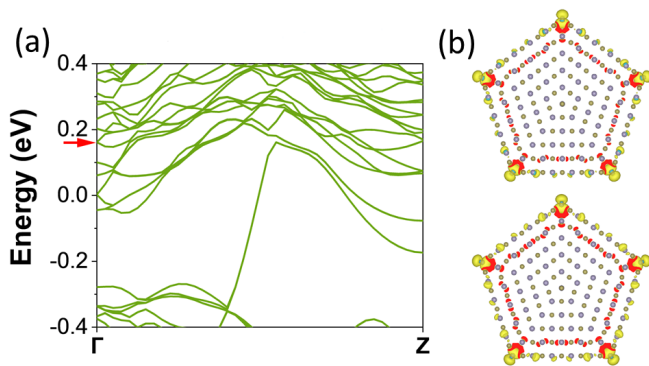


FIG. 6. (a) Band structure of the high-symmetric 5-ring SnTe pentagonal NW with Sn on the twin boundaries. The band connecting valence and conduction band has a positive slope. The charge densities are shown (b) for the degenerate bands at the Γ point. The red arrow in the panel (a) shows the two bands for which we extracted the charge density. The Fermi level is set to zero.

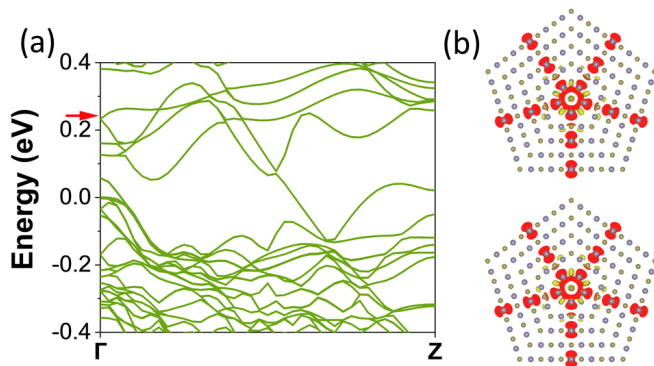


FIG. 7. (a) Band structure of the high-symmetric 5-ring SnTe pentagonal NW with Te on the twin boundaries. The band connecting valence and conduction band has a negative slope. The charge densities are shown (b) for the degenerate bands at the Γ point. The red arrow in the panel (a) shows the two bands for which we extracted the charge density. The Fermi level is set to zero.

at the Γ point. We have a reduction of the band gap at Γ but not at the Z point as a strong indication that the two high-symmetry k -points are different from the topological point of view. In Appendix E, we show that the core chain (CC) of atoms is responsible for the metallicity in the systems. Indeed, the band connecting the valence and conduction electrons disappears when the core chain of atoms is removed within DFT calculations.

In addition to the C_5 symmetry of the global system, it was shown that also the local C_4 symmetry is relevant. Since the preservation of local C_4 symmetry in the region among the twinning is crucial for the observation of the higher-order topology⁹, we study the band structure of the pentagonal NWs with $[110]$ orientation and perfect local C_4 symmetry (without structural relaxation). We define this crystal structure without structural re-

laxations as a high-symmetric pentagonal NW. We show the electronic band structures and charge densities for the most symmetric 5-ring SnTe pentagonal NW with Sn and Te on the twin boundaries in Fig. 6 and Fig. 7. In the band structure of Fig. 6(a) and Fig. 7(a) we observe a two-times degenerate band connecting the valence and conduction band with a positive slope for the Sn-twin boundary and negative slope for the Te-twin boundary. In the case of the Te-twin boundary, we calculate the charge density at the Γ point associated with the band connecting valence and conduction in Fig. 7(b). Its charge is shared between the CC and the Sn atoms on the 5 mirror planes. Supported by the results presented in the model Hamiltonian, we assume that a similar state is present also in the Sn twin boundary NWs but in the conduction band and more hybridized with other bands.

To gain further insight, we perform tight-binding calculations using the model Hamiltonian for a section of the SnTe pentagonal NWs. The tight binding model was reported in previous literature^{47,61} and it was derived from the Shiozaki-Sato-Gomi (SSG) model⁸⁸. We use as a section the mirror plane shown in Fig. 8(a) for a minimal model of the experimental system where the CC acts as a termination defect of the SSG model. In Fig. 8(b), the results for the Sn twin boundary describe a metallic band connecting the valence and conduction band associated with the CC. Even if this band is quite localized in the CC, the hybridization with the shell of the NWs described by the hopping t_3 is extremely relevant. Indeed, without the coupling between core and shell, the metallic band disappears as we can see in Fig. 8(c). Exchanging anion and cation to change the twin boundary, we obtain a band structure for the Te twin-boundary shown in Fig. 8(d). With the Te twin boundary, we obtain the CC state to have a negative slope. Fig. 8(e) describes a simpler model with periodicity along the z -direction that further confirms the relevance of the CC as a termination defect of the SSG model for the formation of the metallic bands in pentagonal NWs. Basically, in both twin boundary cases, the CC band connects the valence and conduction bands enforcing the metallicity even in the ultrathin limit. Therefore, the pentagonal NWs are intrinsic core-shell NWs composed of a single material with a metallic chain in the core and an insulating cubic SnTe shell. Core and shell are electronically and structurally different but have the same constituent elements and stoichiometry.

C. Topological electronic states in the core chain of the pentagonal nanowires

Regarding the topological properties, we analyze two aspects of the pentagonal nanowires. In this subsection, we analyze the topological properties related to the core chain, while in the next subsection, we report the signature of the topological properties related to the fractional charge and hinge states.

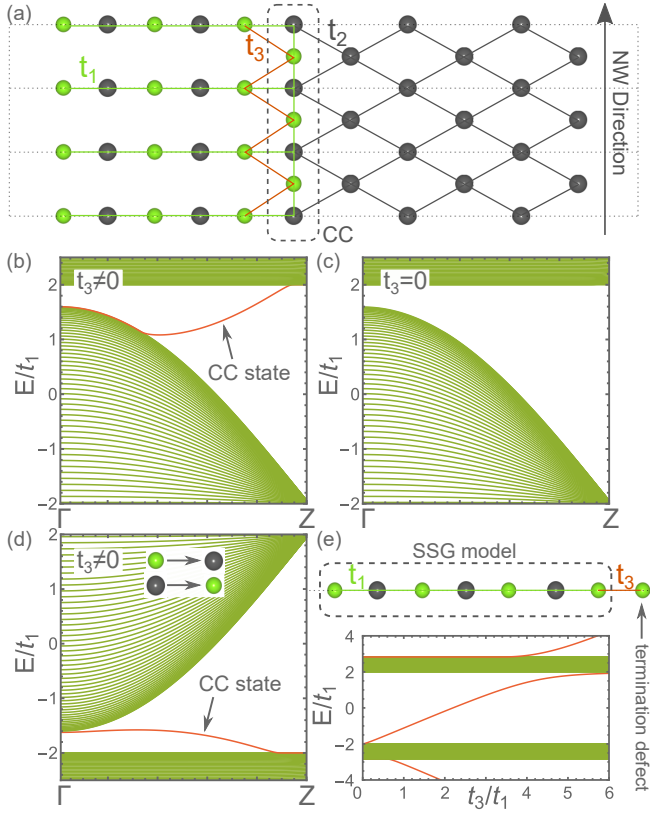


FIG. 8. Effective SSG-like ribbon model, the gray/green dots represent Sn and Te atoms with opposite on-site potentials $\pm m$ defined in the model⁴⁷. (a) The transverse cross-section of the NW with the CC. Its length is equal to twice the number of rings. (b-c) The spectra of the ribbon system are periodic in the NW direction. In case (b) there is a non-vanishing hopping amplitude t_3 and we find a state strongly localized at the CC shown as a red line. In case of lack of this t_3 hopping (c) we do not find the band connecting valence and conduction band. (d) Same as (b) reversing anion and cation, in both (b) and (d) the Fermi level crosses the red line coming from the CC. (e) The minimal SSG model with termination defect and its spectrum showing end-states. The parameters are: $m = 2t_1$, $t_2 = t_3 = 0.9t_1$.

The electronic properties of the core chain were understood using a simplified SSG model Hamiltonian derived from a ribbon of a topologically non-trivial model with nonsymmorphic chiral Z_2 invariant⁸⁹. This model (known also as the Rice-Mele model) was used also to study the presence of topological midgap corner modes in n -fold rotational symmetric chiral insulators to investigate the existence of a HOTI protected by rotational symmetry⁹⁰. The cross-section of the NW that was used for the model Hamiltonian is shown in Fig. 8(a), with the three hopping parameters of the model named as t_1 , t_2 and t_3 . When the hopping t_3 is zero, there are no bands connecting the valence and conduction band and the system is an insulator as shown in Fig. 8(c). When t_3 is different from zero, this model gives electronic states inside the gap connecting the valence and conduction bands

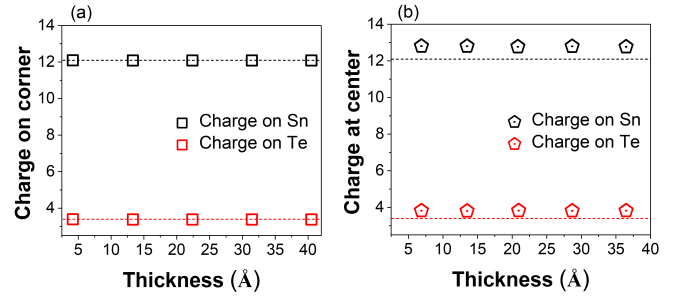


FIG. 9. Total charge on Sn and Te atoms as a function of thickness for the (a) trivial cubic NWs and (b) [110] pentagonal NWs. In the case of cubic systems, the charges are calculated for the corner atoms, whereas for pentagonal structures the charges for the core atoms are considered. The dashed horizontal lines represent the values of charges in the bulk SnTe, i.e. black for Sn and red for Te.

resulting in a symmetry-enforced metallic phase. In the case of Sn on the twin boundary shown in Fig. 8(b), the connecting band has a positive slope while has a negative slope in the case of Te on the twin boundary plotted in Fig. 8(d). The robustness of this symmetry-enforced metallic phase was confirmed also by linear scaling DFT calculations (Appendix F) and by DFT calculations of the NWs under isotropic pressure (Appendix G). These results demonstrate that the electronic properties critically depend on the composition of the CC. The minimal model that reproduces this metallic phase is a SSG model with a termination defect as shown in Fig. 8(e). Note that a pure SSG model without termination defects exhibits no end-states⁸⁹. This is because the termination of the system breaks the nonsymmorphic chiral symmetry that protects the Z_2 topological invariant. However, in the presence of the topological invariant, there is charge accumulation at the edges, in strict analogy to the 1D systems with inversion symmetry⁹¹. We find that with termination defect such accumulation can again lead to the appearance of the end-states.

D. Signature of fractional charge and higher-order topology in pentagonal nanowires

Now, we move to describe the signatures of higher-order topology as the hinge states. The hinge states for SnTe cubic nanowires (grown along the [001] orientation presenting a square section) were observed at a given k -point that was close to the edge of the Brillouin zone^{61,66}. In the case of the Sn twin boundary, we analyzed the charge density at the Γ point in 6(b). Localized charge densities are visible at the corners of the 5-ring pentagonal NW. We surmise that this state will evolve in the localized higher-order topological state once the thickness of the shell is large enough to generate the TCI state of SnTe. While there exist recent studies focused on higher-order topology in finite systems in the xy plane, addi-

tional studies are necessary for the higher-order topology in NWs that are periodic along the z -direction and finite in the xy plane.

In addition to hinge states, another feature of the higher-order topology is the presence of a fractional charge at the center. Fig. 9(a) and 9(b) show the charge for the SnTe cubic and pentagonal NWs, respectively. We report for comparison also the charge in the bulk SnTe. The charges on both Sn and Te of the CC substantially increase with respect to the charge in the bulk and are constant as a function of the thickness. This excess of charge could be associated with the fractional charge appearing in the presence of disclinations. The fractional charge can be observed with and without topology. Fractional charge and higher-order topology are strongly developed in 2D materials but there are less evident in NWs. We leave it to future studies to provide for a deeper explanation of the fractional charge. The interplay between the topological properties from the core and from the shell will be described elsewhere.⁹²

IV. CONCLUSIONS

We have synthesized ionic pentagonal NWs of $\text{Pb}_{1-x}\text{Sn}_x\text{Te}$ with smooth texture devoid of imperfections. Within a semiclassical approach, the pentagonal crystal structure is stabilized by an interplay between the ionic bond and the covalent bond. Within a full quantum approach, we have demonstrated that the pentagonal phase of the SnTe NWs is a metastable phase close in energy to the ground state which is the cubic structure. The pentagonal NWs are an intrinsic core-shell system where the core and shell have different structural, electronic and topological properties. The pentagonal NWs with $[110]$ orientations are metallic due to the presence of a single band connecting the conduction and valence bands coming from the one-dimensional disclination in the core of the NW. This connecting band clearly comes from the one-dimensional disclination and it is related to the properties of the topological SSG model. We have found an excess charge in the center that could be associated with a fractional charge. We have calculated the charge in the real space related to the degenerate electronic states at the Γ point and we find that these states are associated with higher-order topological states at the hinges of the NWs. The pentagonal NWs are a platform for higher-order topology and fractional charge. These pentagonal NWs represent a unique case of intrinsic core-shell NWs with distinct structural, electronic and topological properties between the core and the shell.

ACKNOWLEDGMENTS

We thank T. Dietl, C. Ortix, R. Buczko and S. Samadi for useful discussions. The work is supported by the Foundation for Polish Science through the International

Research Agendas program co-financed by the European Union within the Smart Growth Operational Programme (Grant No. MAB/2017/1). W.B. acknowledges support from Narodowe Centrum Nauki (NCN, National Science Centre, Poland) Project No. 2019/34/E/ST3/00404. J.S. and S.K. acknowledge support from the National Science Centre Poland through the projects 2019/35/B/ST3/03381 and 2019/35/B/ST5/03434. C.M.C. and S.S. thank Carl Tryggers Stiftelsen (CTS 20:71) and the Swedish Research Council (VR 2021-04622) for financial support. We acknowledge the access to the computing facilities of the Interdisciplinary Center of Modeling at the University of Warsaw, Grant g91-1418, g91-1419 and g91-1426 for the availability of high-performance computing resources and support. We acknowledge the CINECA award under the ISCRA initiative IsC99 "SILENTS", IsC105 "SILENTSG", IsB26 "SHINY" and IsB27 "SLAM" grants for the availability of high-performance computing resources and support. We acknowledge the access to the computing facilities of the Poznan Supercomputing and Networking Center Grant No. 609 (pl0223-01) and pl0267-01. The computations at Linnaeus University were enabled by resources provided by the National Academic Infrastructure for Supercomputing in Sweden (NAISS) at Dardel partially funded by the Swedish Research Council through grant agreement no. 2022-06725.

Appendix A: Experimental setup

$\text{Pb}_{1-x}\text{Sn}_x\text{Te}$ NWs were grown by molecular beam epitaxy technique in a home-built system equipped with SnTe, Pb and Te solid sources. We used commercial (Azelis, France) both (100)- and (111)-oriented p-Si substrates covered with a relatively thin oxide layer (up to 10 Å) such that we observed slight streaky reflection high-energy electron diffraction (RHEED) patterns even without any surface preparation. Covering the surface with an amorphous SiO_x layer prevents deposition directly on monocrystalline silicon. On the other hand, these oxides support the mobility of the adatoms on the surface. To uncover Si, the etching procedure in HF was employed. Different solutions of acid (from 8% to 40%), as well as various times of etching (up to 2 min), were applied resulting in different oxides covering stages. The aim was to achieve separated pinholes in oxide which can play the role of the base for the nucleation center. Before loading into load-lock the freshly etched Si substrates were kept in ethanol to protect them against the air. Instead of the typically exploited vapor-liquid-solid (VLS) mode of growth effective for IV-VI, e.g. using Au nanodroplets as a catalyst⁹³, we applied vapor-solid (VS) mode. The growth temperature was in the range from 450 °C to 500 °C. The SnTe/Pb molecular beam flux ratio was kept to obtain $x \approx 0.50 \pm 0.05$ in $\text{Pb}_{1-x}\text{Sn}_x\text{Te}$. The total molecular flux used to grow NWs corresponds to the rate of

growth for layers from 0.1 Å/s to 0.2 Å/s. This results in NWs longer than 1 μm and the rate of NWs growth higher than 0.5 μm/h. Diameters of the NWs show relatively wide distribution from the smallest around 15 nm to even 200 nm with the maximum at approximately 40-80 nm. Under these conditions both types of NWs are observed, i.e., exhibiting four-fold and five-fold symmetry of cross-section (see Fig. 1a).

SEM observations were made using Scanning Electron Microscope ZEISS Auriga - CrossBeam Workstation, images were made at 5 kV with magnification from 10k to 300k x. The images show that the length of the NWs varies from 0.7 μm to 3 μm, and the width of the structures ranges between 40-150 nm. The surface density is from 0.1 to even 5 μm⁻¹. On the substrate, we observed five-fold NWs with greater amounts, less often four-fold NWs. Structures are symmetrical and well-shaped with visible blocks. The surface of the NWs was smooth without any imperfections. Structural properties of the Pb_{1-x}Sn_xTe NWs were examined using FEI-Titan 80-300 transmission electron microscope operating at 300 kV, equipped with an image corrector and HAADF scanning transmission electron microscopy detector. The cross-sectioned NWs were prepared with the Thermo Scientific's Helios G1 NanoLab DualBeam 600 Scanning Electron Microscope, with FIB (Focused Ion Beam)- resolution of 5.0 nm at 30 kV, and lift-off procedure for cross-sections with an Omni-Probe nanomanipulator. The cross-sectioned NWs were investigated in the zone axis [110] which is parallel to the NWs growth axis, in scanning transmission electron microscopy as well as in high-resolution transmission electron microscopy mode. The five-fold symmetry was confirmed, and the (111) planes twin boundaries were visible as well as brighter areas on the twin. These areas are related to strain fields that are visible to distinguish for observations under camera length 0.230 m. EDS determined the averaged elemental ratio as Sn:Pb = 55:45 (~1:1).

Appendix B: Computational details

Electronic structure calculations were performed within the framework of the first-principles density functional theory based on plane wave basis set and projector augmented wave method using VASP⁹⁴ package. The structural relaxations are performed without SOC, while all the band structure calculations of the main text are fully relativistic by considering SOC, a plane-wave energy cut-off of 250 eV has been used. As an exchange-correlation functional, the generalised gradient approximation of Perdrew, Burke, and Ernzerhof has been adopted⁹⁵. We have performed the calculations using 1×1×12 k-points centered in Γ. The electronic band structures are computed with 60 k-points between the Γ and Z direction. The convergence criterion for the force is considered to be 0.01 eV/Å, while 10⁻⁵ eV of energy tolerance is taken for structural relaxation.

In the high-symmetric structure, we study the systems without structural relaxation to study the system with perfect C₄ symmetry in the regions among the twinings.

Appendix C: Semiclassical approach to describe the stability of ionic pentagonal NWs

Since the pentagonal geometry is poorly studied, we also calculated some semiclassical quantities to unveil the reasons for its structural stability. For instance, the Madelung constant and the particle density for three types of polygons such as cube, pentagon, and hexagon are calculated. Finally, we combine both the properties in one plot showing that the pentagonal NWs can be formed in case of an interplay between ionic and covalent bonds.

The three types of polygons considered are shown in Fig. 10. Two types of atoms with different atomic radii are studied and general equations for particle density in two dimensions (2D) are used. The atoms are positioned on the sides and corners of the polygon, the size of the side atoms (r) is variable and smaller than the corner atoms (R). Hence, two regions are studied i.e. $r < r_c$ and $r > r_c$. Here r_c is the critical value of the radius for which the side atom touches the corner one and the density becomes maximum. The general formula for the particle density D_N in the case of NWs with a polygonal section having N sides (N is 4, 5 and 6 for the square, pentagon and hexagon respectively) can be written as;

$$D_N = \frac{\text{Area of occupancy of atoms}}{\text{Total area of the Polygon with N sides}}$$

$$D_N(x) = \begin{cases} \frac{\pi}{4 \sin(\frac{2\pi}{N})} (1 + x^2) & \text{if } 0 < x < x_c \\ \frac{\pi}{2} \tan(\frac{\pi}{N}) \left(1 - \frac{2x}{(1+x)^2}\right) & \text{if } x > x_c \end{cases} \quad (C1)$$

We define $x=r/R$ where r is the radius of the side atoms and R is the radius for the atom at the corners. The particle density $D_N(x)$ reaches a maximum at a critical value $x=x_c$ and afterward starts to decrease. In the cubic environment, the particle density is calculated to be 0.785 for $x=0$ ($r=0$), while it is increased to 0.919 if the radius of the atom located on the side of the polygon approaches the critical value x_c by touching the corner atoms. However, the density again decreases for $x > x_c$ and becomes 0.785 when $r=R$. An almost similar trend is followed by pentagons and hexagons; Following these equations, the particle densities at $r=0$ are reported in Table I. We got the highest density for the hexagonal structure, lowest for the cubic, and intermediate for the pentagon when $r=0$. The hexagonal structure possesses the highest particle density revealing that the covalent bond is favorable in this case, which means more covalent character pushes the system to stay in the hexagonal phase.

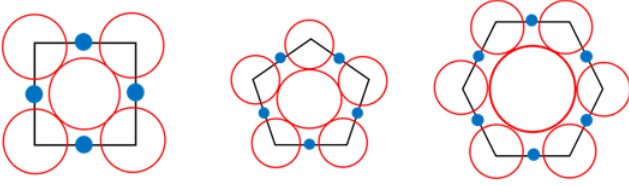


FIG. 10. Three types of polygon i.e. cubic, pentagon and hexagon considered to calculate the particle density and Madelung constant. The atoms are represented by circles. The N red atoms on the vertices have a radius of R , while the N blue atoms on the sides of the polygons have a radius of r . The size of the red atom in the middle is defined to be tangent to the atoms on the vertices and maximize the area occupied by the red atoms.

Polygon	Particle density	Madelung constant
Cube	0.785	1.172
Pentagon	0.825	0.694
Hexagon	0.906	0.464

TABLE I. Particle density and Madelung constant calculated for the cubic, pentagonal, and hexagonal structures. We assume $Q=d=1$.

The Madelung constant determines the electrostatic potential for a single ion in a crystal by approximating the ions with point charges. We calculate the Madelung constant for cube, pentagon, and hexagon. Generally, the Madelung constant is defined as:

$$M_N = \sum_j \frac{z_j}{r_{ij}}$$

where z_j is the number of j -th ions, r_{ij} is the distance between the ions with $N=4, 5,$ and 6 for the cubic, pentagonal, and hexagonal structures, respectively. Considering Q (opposite for the two atoms) as the charge and d as the distance between the two atoms, in the case of a cubic structure, we have:

$$M_4 = \frac{Q}{d} \left(4 - \frac{4}{\sqrt{2}} \right) = 1.172 \frac{Q}{d}$$

In the case of a pentagonal structure:

$$M_5 = \frac{Q}{d} \left(\frac{5\sqrt{10-2\sqrt{5}}}{\sqrt{5}+1} - \frac{5\sqrt{10-2\sqrt{5}}}{4} \right) = 0.694 \frac{Q}{d}$$

while for the hexagonal structure:

$$M_6 = \frac{Q}{d} \left(2\sqrt{3} - 3 \right) = 0.464 \frac{Q}{d}$$

The value of the Madelung constant is very crucial in the case of ionic bonds. As expected, we got the highest

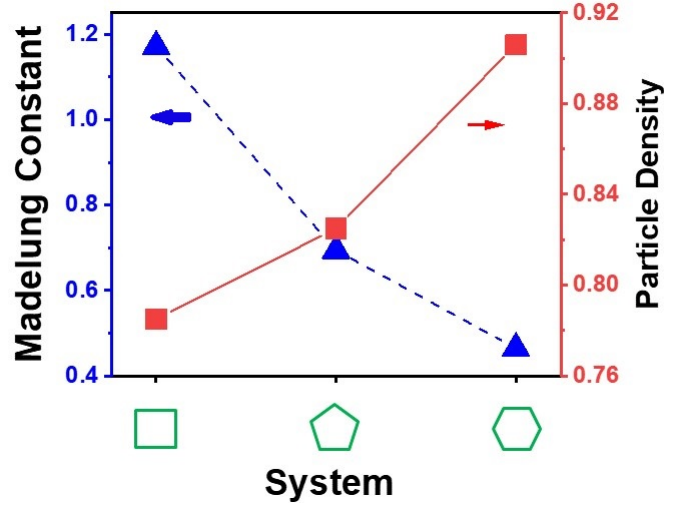


FIG. 11. Particle density (on the right y-axis, red) and Madelung constant (on the left y-axis, blue) calculated for the cubic, pentagonal, and hexagonal structures. The pentagonal phase bears the intermediate values for both the Madelung constant and particle density.

value of the Madelung constant for the cubic system (1.172) and the lowest (0.464) for the hexagon, while the pentagon bears the intermediate value (0.694). The large value of the Madelung constant for a cubic system indicates the highest contribution to ionicity and implies an ionic insulator scenario, which favors the system to be in the cubic phase.

This manifestation of the highest Madelung constant and lowest particle density for the cube indicates the dominance of ionic character in the cubic phase, while the lowest Madelung constant and highest particle density for the hexagonal structure indicate that the system presents a more covalent character in this phase. On the other hand, intermediate values of Madelung constant and particle density for the pentagonal shape (see Fig. 11) reveal the contribution of both the ionic and covalent characters in the bond formation, which implies that if the bond is partially ionic and partially covalent, the pentagonal phase is expected to be the most stable. In the NWs based on lighter elements such as Se and Sn, the bonds would be more ionic, therefore we expect to be less likely to form a pentagonal crystal structure. Therefore, NWs based on Pb and Te would be more likely to form pentagonal NWs.

To summarize, from a semiclassical point of view, we understand that the interplay between covalent and ionic bonds favors the formation of pentagonal NWs. The quantum calculations reported in Section III of the main text demonstrated that the pentagonal NWs are metastable with the ground state being the cubic NWs. The difference between the ground state energies of cubic and pentagonal NWs becomes very small for thick

NWs paving the way for the experimental formation of pentagonal NWs.

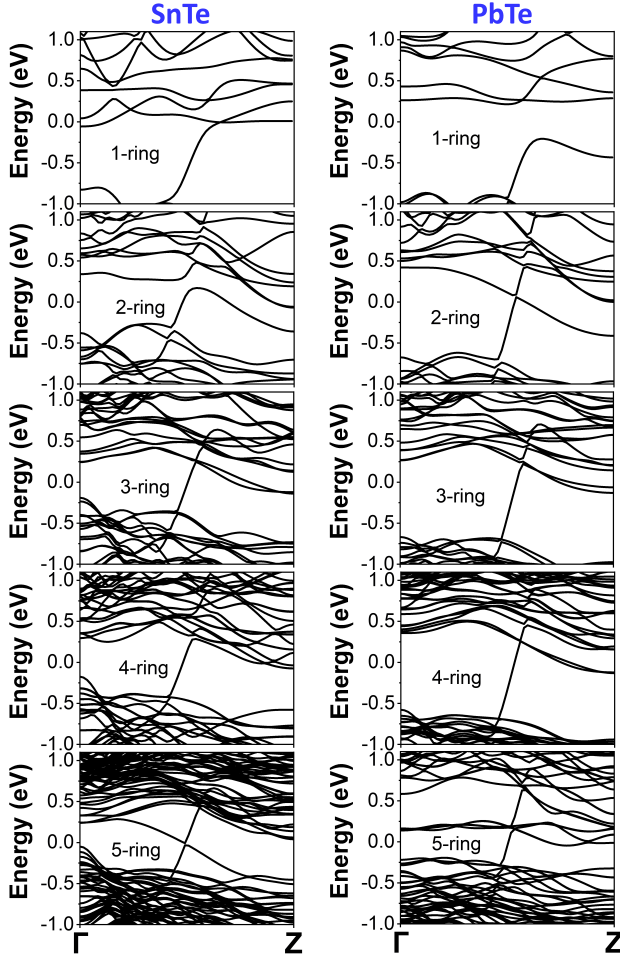


FIG. 12. Band structures of SnTe and PbTe pentagonal NWs in the $\Gamma - Z$ direction grown along $[110]$ with cationic twin-boundaries without SOC. (Left panel) SnTe NWs, (right panel) PbTe NWs. One can see a band in most cases, which connects the valence and conduction electrons giving rise to metallicity. The Fermi level is set to zero.

Appendix D: Band structure of the $[110]$ pentagonal SnTe and PbTe NWs without SOC

In Fig. 12 we show the band structures of these systems without considering SOC interaction; here, both the compounds manifest bands that connect valence and conduction regions except 1-ring PbTe NW, which has an indirect band gap of 0.423 eV. The band connecting valence and conduction at the Γ point is in the conduction band and goes in the valence band increasing k as opposite to the pentagonal NW with $[001]$ orientation. In Appendix E, we show that the core chain is responsible for the metallicity in the systems. Indeed, the band connecting the valence and conduction electrons disap-

pears when the core chain of atoms is removed. Therefore, this band connecting valence and conduction is not related to topological properties since is not a surface band. This band, coming from the one-dimensional core chain, is composed of p_z orbitals of Sn and Te with a very short distance, therefore it would be very difficult to reproduce within the tight-binding models based on a bulk cubic environment with the normal lattice constant. The central atoms (a Sn and Te atom in the unit cell) have around 0.5 electrons more than other atoms, while the first and second-ring atoms have a little less charge of around 0.01 electrons. These 0.5 electrons are due to the different structural environments of the CC or to the fractional charge.

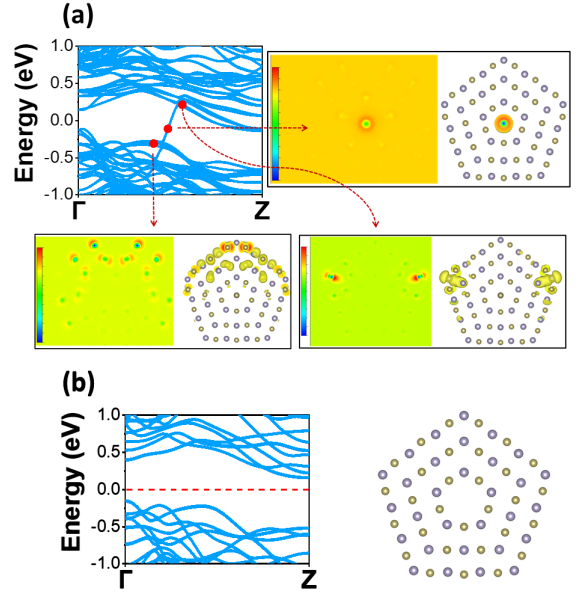


FIG. 13. (a) Band decomposed charge density obtained at different points along the $\Gamma - Z$ direction for the pentagonal NWs oriented in $[110]$. The charge density is distributed in the center of NW in real space when it is not hybridized (indicated by the red dot in the middle). (b) Band structure of the 3-ring pentagonal NW without the core chain, the band connecting the valence and conduction electrons disappears.

Appendix E: Removing the core chain

Here, we calculate the band decomposed charge density at different k -points along the $\Gamma - Z$ direction for the SnTe pentagonal NWs oriented along $[110]$. To check the influence of the core chain on the electronic structure, we show the band decomposed charge density in Fig. 13. The charge density for the band connecting the valence and conduction sectors is distributed in the center of NW in real space when we consider a point in the middle of this band, namely not hybridized. Instead, when we take points where this band is hybridized with other electronic bands, the charge density is distributed

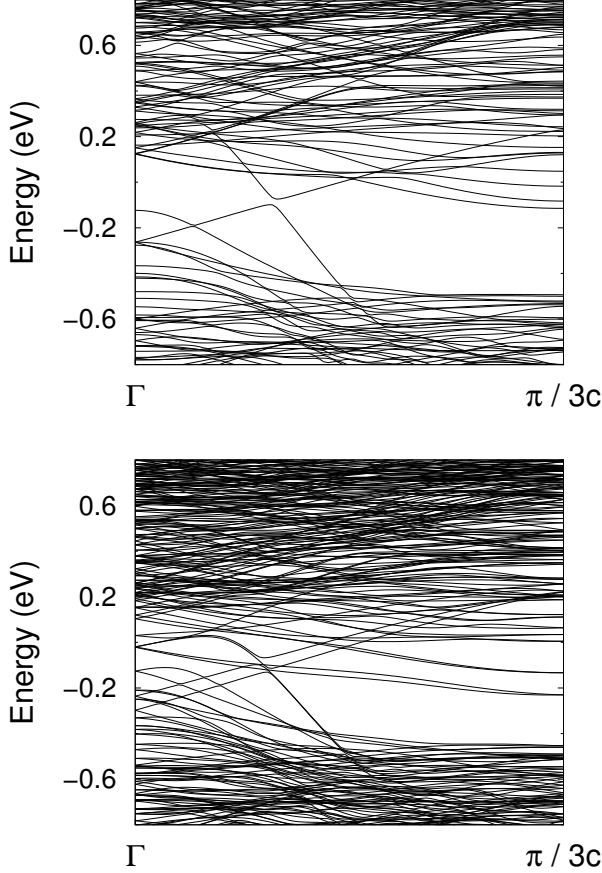


FIG. 14. Band structure for the optimized 5-ring pentagonal NW with Sn-twin boundary using ONETEP. The top panel is without SOC, while the bottom panel is with SOC. This figure should be compared with Fig. 5 of the main text.

in other regions as well, as shown in Fig. 13a). These results clearly indicate that the core chain is responsible for the metallicity in the systems. Further confirming this claim, we removed the core chain of the 3-ring pentagon (the remaining crystal structure is composed of only atoms in a NaCl-phase environment with 6 nearest neighbors) and calculated its band structure as illustrated in Fig. 13b). The band connecting the valence and conduction electrons disappears when the core chain of atoms is removed. The pentagonal SnTe NW without the core chain becomes a simple band insulator as expected for SnTe NWs with a cubic environment in the ultrathin limit. We observe the same behavior also for the [001] pentagonal NWs.

Appendix F: Reproducing the electronic structure within the ONETEP code

To double-check the results obtained within VASP, we perform electronic structure calculations with a DFT code that uses a different basis for the charge density as

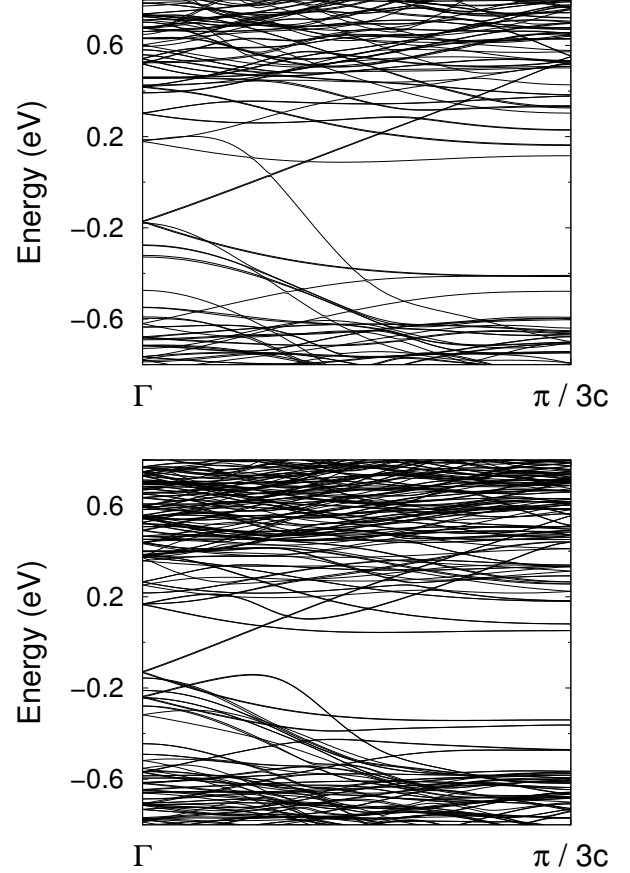


FIG. 15. Band structure for the optimized 5-ring pentagonal NW with Te-twin boundary using ONETEP. The top panel is without SOC, while the bottom panel is with SOC. This figure should be compared with Fig. 5 of the main text.

ONETEP^{96,97}. The computational framework was presented in a previous paper⁷¹. The results are reported in Figs. 14 and 15 for the 5-rings optimized structure of SnTe with Sn and Te twin boundaries, respectively. The results for the 5-rings of SnTe with high-symmetry structure and with Sn and Te twin boundaries are reported in Figs. 16 and 17, respectively. In order to do this, we repeat the unit cell three times along the c -axis, this produces a triple downfolding of the band structure. Due to the downfolding, the metallic band has an opposite inclination with respect to the VASP but the results are strongly consistent with the VASP results. The SnTe band structures within ONETEP show a slightly larger gap for the shell bands as it happens in the cubic NWs⁷¹.

Appendix G: Band structure under applied pressure

The study of the topological properties in the cubic NWs is extremely demanding computationally because of the thickness dependence of the topology. Indeed, we need to have a large thickness to reach the topolog-

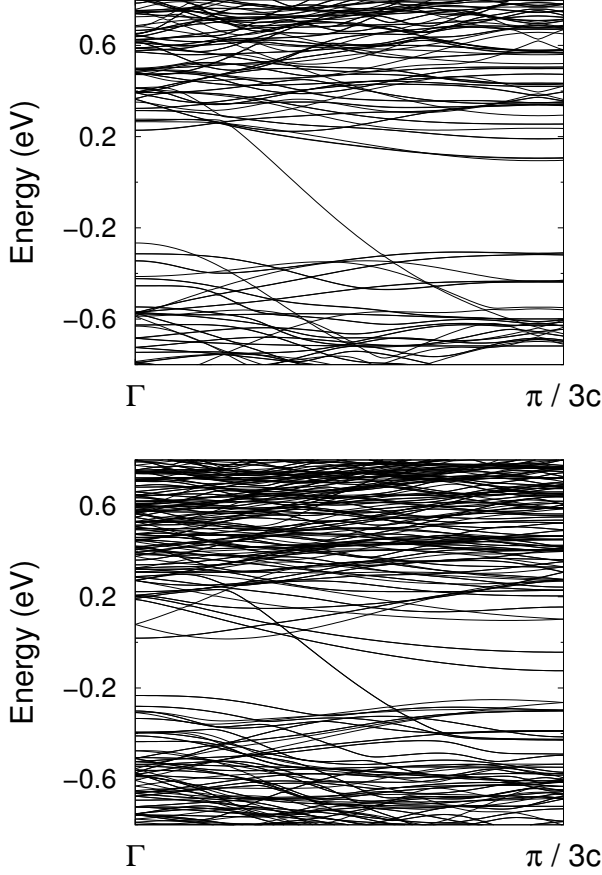


FIG. 16. Band structure for the high-symmetric 5-ring pentagonal NW with Sn-twin boundary using ONETEP. The top panel is without SOC, while the bottom panel is with SOC. This figure should be compared with Fig. 6 of the main text.

ical phase in the cubic NWs. In cubic bulk SnTe and PbTe compounds, the effect of the compression pushes the SnTe material-class compounds toward the topological region of the phase diagram. Since our thin NWs are extremely thin the cubic shell region is in a trivial regime, we apply compression in order to observe the topological transition in the shell region. The transition of the cubic shell from the trivial to the topological phase for the pentagonal NWs should go through a closure of the trivial band gap at one or both high-symmetry points Γ and Z . The effect of compression on the electronic band structures of symmetric 5-ring SnTe pentagonal NW with Te

on the twin boundaries is shown in Fig. 18. We notice a reduction of the band gaps at Γ and Z , the systems become more metallic as the compression is increased due to the increasing of the bandwidth as happens in bulk phases²³, however, no closure of the gap at Γ or Z is observed. Even if the thickness is too thin to develop a topological phase in the cubic SnTe, we have the connection between valence and conduction due to the core chain persisting at every pressure.

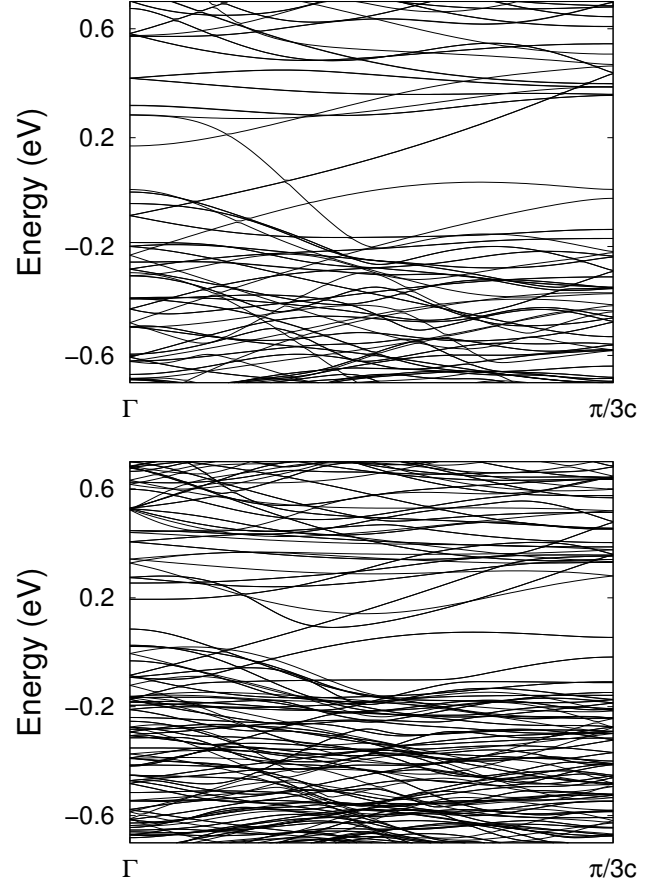


FIG. 17. Band structure for the high-symmetric 5-ring pentagonal NW with Te-twin boundary using ONETEP. The top panel is without SOC, while the bottom panel is with SOC. This figure should be compared with Fig. 7 of the main text.

* autieri@magtop.ifpan.edu.pl

¹ B. Xie, H.-X. Wang, X. Zhang, P. Zhan, J.-H. Jiang, M. Lu, and Y. Chen, *Nature Reviews Physics* **3**, 520 (2021).

² G. van Miert and C. Ortix, *Phys. Rev. B* **98**, 081110 (2018).

³ S. H. Kooi, G. van Miert, and C. Ortix, *Phys. Rev. B* **102**, 041122 (2020).

⁴ Y. Xu, Z. Song, Z. Wang, H. Weng, and X. Dai, *Phys. Rev. Lett.* **122**, 256402 (2019).

⁵ R. Islam, S. Mardanya, A. Lau, G. Cuono, T.-R. Chang, B. Singh, C. M. Canali, T. Dietl, and C. Autieri, *Phys. Rev. B* **107**, 125102 (2023).

⁶ N. Pournaghavi, M. F. Islam, R. Islam, C. Autieri, T. Dietl, and C. M. Canali, *Phys. Rev. B* **103**, 195308 (2021).

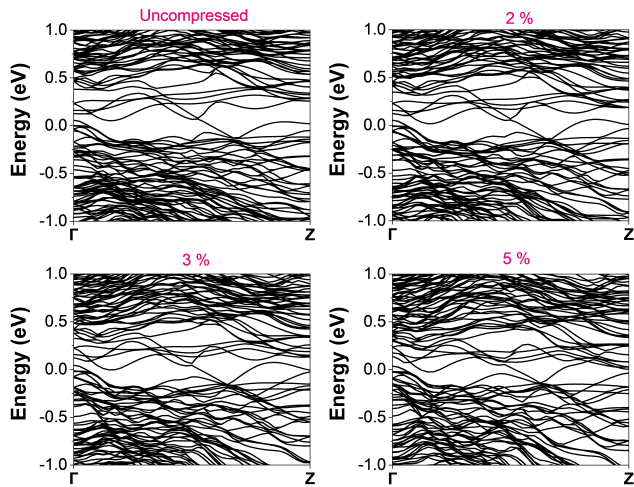


FIG. 18. Band structures of the high-symmetric 5-ring SnTe pentagonal NW with Te on the twin boundaries for the uncompressed and compressed systems. The calculations were performed with SOC. The Fermi level is set to zero.

- ⁷ F. Schindler, Z. Wang, M. G. Vergniory, A. M. Cook, A. Murani, S. Sengupta, A. Y. Kasumov, R. Deblock, S. Jeon, I. Drozdov, H. Bouchiat, S. Guéron, A. Yazdani, B. A. Bernevig, and T. Neupert, *Nature Physics* **14**, 918 (2018).
- ⁸ F. Schindler, A. M. Cook, M. G. Vergniory, Z. Wang, S. S. P. Parkin, B. A. Bernevig, and T. Neupert, *Science Advances* **4** (2018), 10.1126/sciadv.aat0346.
- ⁹ M. Geier, I. C. Fulga, and A. Lau, *SciPost Phys.* **10**, 092 (2021).
- ¹⁰ F. Schindler, S. S. Tsirkin, T. Neupert, B. Andrei Bernevig, and B. J. Wieder, *Nature Communications* **13**, 5791 (2022).
- ¹¹ W. A. Benalcazar, J. C. Y. Teo, and T. L. Hughes, *Phys. Rev. B* **89**, 224503 (2014).
- ¹² B. Roy and V. Juričić, *Phys. Rev. Res.* **3**, 033107 (2021).
- ¹³ C. W. Peterson, T. Li, W. Jiang, T. L. Hughes, and G. Bahl, *Nature* **589**, 376 (2021).
- ¹⁴ Y. Liu, S. Leung, F.-F. Li, Z.-K. Lin, X. Tao, Y. Poo, and J.-H. Jiang, *Nature* **589**, 381 (2021).
- ¹⁵ Y. Zhang, C. Liu, X. Dai, and Y. Xiang, *Phys. Rev. B* **107**, 214108 (2023).
- ¹⁶ H. Wang, Y. Pei, A. D. LaLonde, and G. J. Snyder, *Advanced Materials* **23**, 1366 (2011).
- ¹⁷ C. Wood, *Reports on progress in physics* **51**, 459 (1988).
- ¹⁸ A. I. Lebedev and I. A. Sluchinskaya, *Ferroelectrics* **157**, 275 (1994).
- ¹⁹ P. Liu, H. J. Han, J. Wei, D. J. Hynek, J. L. Hart, M. G. Han, C. J. Trimble, J. R. Williams, Y. Zhu, and J. J. Cha, *ACS Applied Electronic Materials* **3**, 184 (2021).
- ²⁰ Y. Matsushita, P. Wiannecki, A. T. Sommer, T. Geballe, and I. Fisher, *Physical Review B* **74**, 134512 (2006).
- ²¹ G. P. Mazur, K. Dybko, A. Szczerbakow, J. Z. Domagala, A. Kazakov, M. Zgirski, E. Lusakowska, S. Kret, J. Korczak, T. Story, M. Sawicki, and T. Dietl, *Phys. Rev. B* **100**, 041408(R) (2019).
- ²² L. Fu, *Physical Review Letters* **106**, 106802 (2011).
- ²³ T. H. Hsieh, H. Lin, J. Liu, W. Duan, A. Bansil, and L. Fu, *Nature communications* **3**, 1 (2012).
- ²⁴ A. Lau and C. Ortix, *Phys. Rev. Lett.* **122**, 186801 (2019).
- ²⁵ Y. Tanaka, Z. Ren, T. Sato, K. Nakayama, T. Souma, S. and Takahashi, T. Takahashi, K. Segawa, and Y. Ando, *Nature Physics* **8**, 800 (2012).
- ²⁶ Y. Okada, M. Serbyn, H. Lin, D. Walkup, W. Zhou, C. Dhital, M. Neupane, S. Xu, Y. J. Wang, R. Sankar, F. Chou, A. Bansil, M. Z. Hasan, S. D. Wilson, L. Fu, and V. Madhavan, *Science* **341**, 1496 (2013).
- ²⁷ S.-Y. Xu, C. Liu, N. Alidoust, M. Neupane, D. Qian, I. Belopolski, J. Denlinger, Y. Wang, H. Lin, L. a. Wray, *et al.*, *Nature communications* **3**, 1 (2012).
- ²⁸ P. Dziawa, B. Kowalski, K. Dybko, R. Buczko, A. Szczerbakow, M. Szot, E. Lusakowska, T. Balasubramanian, B. M. Wojek, M. Berntsen, *et al.*, *Nature Materials* **11**, 1023 (2012).
- ²⁹ A. Lusakowski, P. Bogusławski, and T. Story, *Phys. Rev. B* **108**, 125201 (2023).
- ³⁰ L. Fu, C. L. Kane, and E. J. Mele, *Phys. Rev. Lett.* **98**, 106803 (2007).
- ³¹ J. C. Y. Teo, L. Fu, and C. L. Kane, *Phys. Rev. B* **78**, 045426 (2008).
- ³² S. Safaei, M. Galicka, P. Kacman, and R. Buczko, *New Journal of Physics* **17**, 063041 (2015).
- ³³ G. Cuono, G. Hussain, A. Fakhredine, and C. Autieri, *Acta Physica Polonica A* **142** (2022), 10.12693/APhysPolA.142.521.
- ³⁴ R. Rechciński, M. Galicka, M. Simma, V. V. Volobuev, O. Caha, J. Sánchez-Barriga, P. S. Mandal, E. Gollias, A. Varykhalov, O. Rader, G. Bauer, P. Kacman, R. Buczko, and G. Springholz, *Advanced Functional Materials* **31**, 2008885 (2021).
- ³⁵ E. Plekhanov, P. Barone, D. Di Sante, and S. Picozzi, *Phys. Rev. B* **90**, 161108 (2014).
- ³⁶ H. Wang, P. Gopal, S. Picozzi, S. Curtarolo, M. Buongiorno Nardelli, and J. Sławińska, *npj Computational Materials* **6**, 161108 (2020).
- ³⁷ P. Barone, T. c. v. Rauch, D. Di Sante, J. Henk, I. Mertig, and S. Picozzi, *Phys. Rev. B* **88**, 045207 (2013).
- ³⁸ J. Sławińska, F. T. Cerasoli, P. Gopal, M. Costa, S. Curtarolo, and M. B. Nardelli, *2D Materials* **7**, 025026 (2020).
- ³⁹ V. V. Volobuev, P. S. Mandal, M. Galicka, O. Caha, J. Sánchez-Barriga, D. Di Sante, A. Varykhalov, A. Khlar, S. Picozzi, G. Bauer, P. Kacman, R. Buczko, O. Rader, and G. Springholz, *Advanced Materials* **29**, 1604185 (2017).
- ⁴⁰ K. Liu, J. Lu, S. Picozzi, L. Bellaiche, and H. Xiang, *Phys. Rev. Lett.* **121**, 027601 (2018).
- ⁴¹ J. Liu, T. H. Hsieh, P. Wei, W. Duan, J. Moodera, and L. Fu, *Nature materials* **13**, 178 (2014).
- ⁴² J. Liu, X. Qian, and L. Fu, *Nano letters* **15**, 2657 (2015).
- ⁴³ H. Ozawa, A. Yamakage, M. Sato, and Y. Tanaka, *Phys. Rev. B* **90**, 045309 (2014).
- ⁴⁴ J. Liu and L. Fu, *Phys. Rev. B* **91**, 081407 (2015).
- ⁴⁵ O. Arroyo-Gascón, Y. Baba, J. I. Cerdá, O. de Abril, R. Martínez, F. Domínguez-Adame, and L. Chico, *Nanoscale* **14**, 7151 (2022).
- ⁴⁶ P. Sessi, D. Di Sante, A. Szczerbakow, F. Glott, S. Wilfert, H. Schmidt, T. Bathon, P. Dziawa, M. Greiter, M. Neupert, M. Greiter, T. Neupert, G. Sangiovanni, T. Story, R. Thomale, and M. Bode, *Science* **354**, 1269 (2016).
- ⁴⁷ W. Brzezicki, M. M. Wysockiński, and T. Hyart, *Phys. Rev. B* **100**, 121107(R) (2019).
- ⁴⁸ G. Wagner, S. Das, J. Jung, A. Odobesko, F. Küster, F. Keller, J. Korczak, A. Szczerbakow, T. Story, S. S. P.

- Parkin, R. Thomale, T. Neupert, M. Bode, and P. Sessi, *Nano Letters* **23**, 2476 (2023).
- 49 R. Rechciński and R. Buczko, *Phys. Rev. B* **98**, 245302 (2018).
- 50 C. Ortix, *Nature* **589**, 356 (2016).
- 51 Y. Liu, L. S., L. F. F., L. Z. K., T. X., P. Y., and J. J. H., *Nature* **589**, 381 (2021).
- 52 B. Roy and V. Juričić, *Phys. Rev. Res.* **3**, 033107 (2021).
- 53 W. A. Benalcazar, J. C. Y. Teo, and T. L. Hughes, *Phys. Rev. B* **89**, 224503 (2014).
- 54 Y. Chen, Y. Yin, Z.-K. Lin, Z.-H. Zheng, Y. Liu, J. Li, J.-H. Jiang, and H. Chen, *Phys. Rev. Lett.* **129**, 154301 (2022).
- 55 S. S. Yamada, T. Li, M. Lin, C. W. Peterson, T. L. Hughes, and G. Bahl, *Nature Communications* **13**, 2035 (2022).
- 56 S. Samadi, R. Rechciński, and R. Buczko, *Phys. Rev. B* **107**, 205401 (2023).
- 57 J. Shen and J. J. Cha, *Nanoscale* **6**, 14133 (2014).
- 58 E. Z. Xu, Z. Li, J. A. Martinez, N. Sinitsyn, H. Htoon, N. Li, B. Swartzentruber, J. A. Hollingsworth, J. Wang, and S. X. Zhang, *Nanoscale* **7**, 2869 (2015).
- 59 J. Sadowski, P. Dziawa, A. Kaleta, B. Kurowska, A. Reszka, T. Story, and S. Kret, *Nanoscale* **10**, 20772 (2018).
- 60 A. Vasylenko, S. Marks, J. M. Wynn, P. V. C. Medeiros, Q. M. Ramasse, A. J. Morris, J. Sloan, and D. Quigley, *ACS Nano* **12**, 6023 (2018).
- 61 N. M. Nguyen, W. Brzezicki, and T. Hyart, *Phys. Rev. B* **105**, 075310 (2022).
- 62 M. Safdar, Q. Wang, Z. Wang, X. Zhan, K. Xu, F. Wang, M. Mirza, and J. He, *Nano Letters* **15** (2015), 10.1021/nl504976g.
- 63 S. Dad, P. Dziawa, W. Zajkowska-Pietrzak, S. Kret, M. Kozłowski, M. Wójcik, and J. Sadowski, *Scientific Reports* **14**, 589 (2024).
- 64 M. Saghir, A. M. Sanchez, S. A. Hindmarsh, S. J. York, and G. Balakrishnan, *Cryst. Growth Des.* **15** (2015), 10.1021/acs.cgd.5b00577.
- 65 E. Xu, Z. Li, J. A. Acosta, N. Li, B. Swartzentruber, S. Zheng, N. Sinitsyn, H. Htoon, J. Wang, and S. Zhang, *Nano Res.* **9**, 820 (2016).
- 66 R. M. Skiff, F. de Juan, R. Queiroz, S. Mathimalar, H. Beidenkopf, and R. Ilan, *SciPost Phys. Core* **6**, 011 (2023).
- 67 W. Song, Y. Wang, W. Miao, Z. Yu, Y. Gao, R. Li, S. Yang, F. Chen, Z. Geng, Z. Zhang, S. Zhang, Y. Zang, Z. Cao, D. E. Liu, R. Shang, X. Feng, L. Li, Q.-K. Xue, K. He, and H. Zhang, *Phys. Rev. B* **108**, 045426 (2023).
- 68 J. Jung, S. G. Schellingerhout, M. F. Ritter, S. C. ten Kate, O. A. van der Molen, S. de Loijer, M. A. Verheijen, H. Riel, F. Nichele, and E. P. Bakkers, *Advanced Functional Materials* **32** (2022), 10.1002/adfm.202208974.
- 69 S. Frolov, *Nature* **592**, 350 (2021).
- 70 R. S. Shukla, V. B. Zala, S. K. Gupta, and P. N. Gajjar, *J. Mater. Chem. C* **10**, 15601 (2022).
- 71 G. Hussain, K. Warda, G. Cuono, and C. Autieri, (2023), arXiv:2308.15358 [cond-mat.mes-hall].
- 72 Y. Shen and Q. Wang, *Physics Reports* **964**, 1 (2022).
- 73 S. Winczewski and J. Rybicki, *Computational Materials Science* **201**, 110914 (2022).
- 74 M. Bykov, E. Bykova, A. V. Ponomareva, F. Tasnádi, S. Chariton, V. B. Prakapenka, K. Glazyrin, J. S. Smith, M. F. Mahmood, I. A. Abrikosov, and A. F. Goncharov, *ACS Nano* **15**, 13539 (2021), pMID: 34355559, <https://doi.org/10.1021/acsnano.1c04325>.
- 75 S. Bravo, J. Correa, L. Chico, and M. Pacheco, *Scientific Reports* **9**, 12754 (2019).
- 76 J. C. González, V. Rodrigues, J. Bettini, L. G. C. Rego, A. R. Rocha, P. Z. Coura, S. O. Dantas, F. Sato, D. S. Galvão, and D. Ugarte, *Phys. Rev. Lett.* **93**, 126103 (2004).
- 77 J. Reyes-Gasga, J. Elechiguerra, C. Liu, A. Camacho-Bragado, J. Montejano-Carrizales, and M. Jose Yacaman, *Journal of Crystal Growth* **286**, 162 (2006).
- 78 M. Antsov, B. Polyakov, V. Zadin, M. Mets, S. Oras, M. Vahtrus, R. Löhmus, L. Dorogin, and S. Vlassov, *Micron* **124**, 102686 (2019).
- 79 P. Sen, O. Gülseren, T. Yildirim, I. P. Batra, and S. Ciraci, *Phys. Rev. B* **65**, 235433 (2002).
- 80 L.-C. Ma and H.-S. Zhao, *Journal of Physics and Chemistry of Solids* **74**, 1115 (2013).
- 81 G. Sainath and B. K. Choudhary, *Materials Research Express* **3**, 125022 (2016).
- 82 E. Pahl, F. Calvo, L. Koči, and P. Schwerdtfeger, *Angewandte Chemie International Edition* **47**, 8207 (2008), <https://onlinelibrary.wiley.com/doi/pdf/10.1002/anie.200802743>.
- 83 K. Adhikari and A. K. Ray, *Journal of Nanoparticle Research* **14**, 816 (2012).
- 84 T. Tarkowski and N. Gonzalez Szwacki, *Solid State Sciences* **142**, 107241 (2023).
- 85 G. Hussain and C. Autieri, In manuscript (2024).
- 86 T. C. van Thiel, J. Fowlie, C. Autieri, N. Manca, M. Šiškins, D. Afanasiev, S. Gariglio, and A. D. Caviglia, *ACS Materials Lett.* **2**, 389 (2020), <https://doi.org/10.1021/acsmaterialslett.9b00540>.
- 87 C. Autieri, *Journal of Physics: Condensed Matter* **28**, 426004 (2016).
- 88 K. Shiozaki, M. Sato, and K. Gomi, *Phys. Rev. B* **91**, 155120 (2015).
- 89 W. Brzezicki and T. Hyart, *Phys. Rev. B* **101**, 235113 (2020).
- 90 G. van Miert and C. Ortix, *npj Quantum Materials* **5**, 63 (2020).
- 91 J.-W. Rhim, J. Behrends, and J. H. Bardarson, *Phys. Rev. B* **95**, 035421 (2017).
- 92 S. Samadi and R. Buczko, In manuscript (2024).
- 93 P. Dziawa, J. Sadowski, P. Dłuzewski, E. Lusakowska, V. Domukhovski, B. Taliashvili, T. Wojciechowski, L. Baczewski, M. Bukala, M. Galicka, *et al.*, *Crystal growth & design* **10**, 109 (2010).
- 94 G. Kresse and J. Furthmüller, *Physical Review B* **54**, 11169 (1996).
- 95 J. P. Perdew, K. Burke, and M. Ernzerhof, *Physical Review Letters* **77**, 3865 (1996).
- 96 C.-K. Skylaris, P. D. Haynes, A. A. Mostofi, and M. C. Payne, *The Journal of Chemical Physics* **122**, 084119 (2005), https://pubs.aip.org/aip/jcp/article-pdf/doi/10.1063/1.1839852/15362896/084119_1_online.pdf.
- 97 J. C. A. Prentice, J. Aarons, J. C. Womack, A. E. A. Allen, L. Andrinopoulos, L. Anton, R. A. Bell, A. Bhandari, G. A. Bramley, R. J. Charlton, R. J. Clements, D. J. Cole, G. Constantinescu, F. Corsetti, S. M.-M. Dubois, K. K. B. Duff, J. M. Escartín, A. Greco, Q. Hill, L. P. Lee, E. Linscott, D. D. O'Regan, M. J. S. Phipps, L. E. Ratcliff, A. R. Serrano, E. W. Tait, G. Teobaldi, V. Vitale, N. Yeung, T. J. Zuehlsdorff, J. Dziedzic, P. D. Haynes, N. D. M. Hine, A. A. Mostofi, M. C. Payne, and C.-K. Skylaris, *The Journal of Chemical Physics* **152**, 174111 (2020), <https://pubs.aip.org/aip/jcp/article->

